ACS APPLIED MATERIALS & INTERFACES

Ag Nanoparticle Embedded TiO_2 Composite Nanorod Arrays Fabricated by Oblique Angle Deposition: Toward Plasmonic Photocatalysis

Yizhuo He,*[†] Pradip Basnet,[†] Simona E. Hunyadi Murph,[‡] and Yiping Zhao[†]

[†]Department of Physics and Astronomy, and Nanoscale Science and Engineering Center, University of Georgia, Athens, Georgia 30602, U.S.A.

[‡]Savannah River National Laboratory, Aiken, SC 29808, U.S.A.

Supporting Information

ABSTRACT: Using a unique oblique angle co-deposition technique, well-aligned arrays of Ag nanoparticle embedded TiO_2 composite nanorods have been fabricated with different concentrations of Ag. The structural, optical, and photocatalytic properties of the composite nanostructures are investigated using a variety of experimental techniques and compared with those of pure TiO_2 nanorods fabricated similarly. Ag nanoparticles are formed in the composite nanorods, which increase the visible light absorbance due to localized surface plasmon resonance. The Ag concentrations and the annealing conditions are found to affect the size and the density of Ag nanoparticles and their optical properties. The Ag nanoparticle embedded TiO_2 nanostructures exhibit enhanced photocatalytic activity compared to pure TiO_2 under visible- or UV-light illumination. Ag plays different roles in assisting the photocatalysis with different light sources. Ag can be excited and can inject electrons to TiO_2, working as an electron donor under visible light. While under UV illumination, Ag acts as an electron acceptor to trap the photogenerated electrons in TiO_2. Due to the opposite electron transfer direction under UV and visible light, the presence of Ag may not result in a greater enhancement in the photocatalytic performance.

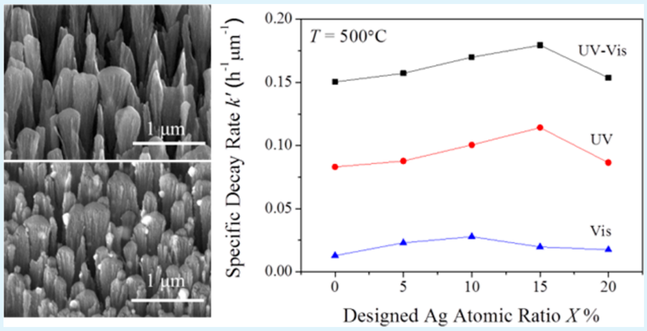

KEYWORDS: *oblique angle co-deposition, nanorods, plasmonic photocatalyst, Ag nanoparticle embedded* TiO_2

1. INTRODUCTION

Nanostructured titanium dioxide (TiO_2) has attracted great attention among various semiconductor photocatalysts due to its promising performance in many applications, including water splitting[1−3] and CO_2 photoreduction.[4−7] However, it is well-known that the large band gap (~3.2 eV) and the fast electron−hole recombination limit the photoresponse spectral range and the practical efficiency of intrinsic TiO_2 as a photocatalyst. Several strategies such as doping with nonmetal (NO_x and N),[8,9] doping with metal (Cr and V),[10−12] dye sensitization,[13] and coupling with other semiconductors[14] have been proposed to circumvent these problems. The addition of noble metal to TiO_2, such as Pt,[15] has been demonstrated as an effective way to improve the photocatalytic efficiency because noble metal can trap the photogenerated electrons in TiO_2 and inhibit the charge recombination process.[16,17]

Recently, plasmonic photocatalysis has been proposed to extend the photocatalytic activity of TiO_2 to the visible light range. Generally, plasmonic photocatalysts are mixtures of semiconductors and noble metal nanoparticles (NPs). The semiconductors usually absorb UV or visible light and then generate electron−hole pairs that will participate in the photocatalytic reaction. The noble metal NPs usually have strong absorption in the visible region due to localized surface plasmon resonance (LSPR). From the energy conversion point of view, if the energy of the absorbed visible light by noble metal NPs can be utilized to improve photocatalytic reaction rates, then the coupled semiconductor−metal system is a plasmonic photocatalyst. There are three possible mechanisms for plasmonic photocatalysts to extend the photocatalytic performance to the visible light range. First, the noble metal nanoparticles can be directly coupled to semiconductors so that the photogenerated electrons or holes due to LSPR absorbance in metal NPs may be transferred to semiconductors, resulting in enhanced photocatalytic performance.[18] However, direct contact of semiconductor with noble metal can also lead to back transfer of charges from semiconductors to noble metal NPs. Another possible mechanism is that when semiconductors and noble metals are spatially separated, the excited noble metal NPs can transfer the absorbed energy to semiconductors in a radiative way through localized interaction of semiconductors with the LSPR-induced enhanced localized electric field.[19] In

Received: August 20, 2013
Accepted: October 29, 2013
Published: October 29, 2013

addition, the heat generated through LSPR absorbance by metal NPs could be a third possible mechanism in some cases. The high absorbance of metal NPs at LSPR wavelength can heat the surroundings locally due to the nonradiative decay of surface plasmons to phonons and can therefore accelerate the photocatalytic reactions by increasing the local temperature around semiconductors.[20]

Among the proposed plasmonic photocatalysts, Ag−TiO_2 composites have been widely studied and prepared by a variety of methods. In many studies, Ag NPs are loaded on the surface of TiO_2 by different techniques, such as radio frequency (RF) sputtering,[21] photodeposition,[22] and the electrostatic force directed assembly (ESFDA) method.[23] Enhancement in photocatalytic activity has been observed with these Ag−TiO_2 samples. However, since most Ag is on the surface of TiO_2, the surface area of TiO_2 exposed to illumination is reduced, and also the interface between Ag and TiO_2 is limited. In order to facilitate the charge-transfer process, the interface between Ag and TiO_2 should be maximized. A better design could be achieved by simply mixing Ag NPs to TiO_2 structures. This has been realized by the sol−gel method.[24,25] However, the sol−gel method usually needs precursors and may have organic residues in the samples. Moreover, a good control over the structure of samples is hard to achieve via the sol−gel method. A better strategy is to make Ag−TiO_2 porous nanostructures directly through physical means.

Oblique angle co-deposition, which combines co-deposition and oblique angle deposition (OAD), has been repeatedly demonstrated as a powerful technique to fabricate well-aligned composite nanostructures.[26−31] OAD is a well-known physical vapor deposition technique in which the vapor flux is incident onto a substrate at a large incident angle (>70°) with respect to the substrate normal. Generally, well-aligned and tilted nanorod arrays are formed due to the geometric shadowing effect. The morphological parameters of the nanorod array such as the tiling angle, nanorod length, nanorod density, and so forth, can be tuned by varying the deposition conditions such as deposition angle, rate, time, and temperature. In co-deposition, two or more materials are evaporated simultaneously and then deposited on the substrates to produce composite materials, of which the composition can be easily controlled by varying the relative ratio of the deposition rates of the two materials. Therefore, by combining OAD and co-deposition, composite nanorod arrays with tunable morphology and composition can be fabricated. Recently, we have successfully fabricated Ag NP embedded MgF_2,[27] Cr-doped TiO_2,[28] CdSe−TiO_2,[29] Si−Cu,[31] and Si−Cu composition graded nanorods[32] by the oblique angle co-deposition (OACD) method. Typically, Ag NPs are embedded in MgF_2 and exhibit LSPR properties, which suggests that it is possible to fabricate TiO_2 nanorods with Ag NPs embedded as a plasmonic photocatalyst using the OACD method.

In this work, Ag NP embedded TiO_2 composite nanorod arrays of various Ag concentrations are prepared by OACD. The structural, optical, and photocatalytic properties are characterized and compared with those of pure TiO_2, which is fabricated by a single-source OAD technique. Ag nanoclusters are found to segregate out of the TiO_2 matrix and form nanoparticles. The size and the density of Ag NPs are greatly affected by the concentrations of Ag and postdeposition annealing condition. These Ag NPs extend the absorbance of the composite nanorods into the visible region. Furthermore, the photocatalytic activity is tested by Methylene Blue (MB) degradation under visible- and UV-light illumination. Ag NP embedded TiO_2 is found to exhibit better catalytic performance compared to intrinsic TiO_2, and the functionality of Ag NPs is different under different illumination.

2. EXPERIMENTAL SECTION

TiO_2 and Ag NP embedded TiO_2 nanorod arrays were fabricated using the OACD technique in a custom-designed vacuum deposition system (Pascal Technology) equipped with two electron-beam evaporation sources. The details of the deposition system can be found elsewhere.[33] Precleaned glass microscopic slides (Gold Seal catalog no. 3010) and Si (100) wafers were used as substrates. Before deposition, the chamber was evacuated to the pressure of 8×10^{-7} Torr. The TiO_2 (99.9%, Kurt J. Lesker) and Ag (99.999%, Kurt J. Lesker) sources were evaporated under a pressure around 5×10^{-6} Torr. The deposition vapor flux was incident onto substrates at an angle of 87° with respect to the substrate normal. Two separate quartz crystal microbalances (QCMs) were used to independently monitor the deposition rates r_{Ag} and r_{TiO_2}, respectively, during the deposition. By changing the relative ratio of r_{Ag} and r_{TiO_2}, the atomic ratio of Ag in the composite X % could be tuned following the relation

$$X/(100 - X) = (\rho_{Ag} r_{Ag}/M_{Ag}) : (\rho_{TiO_2} r_{TiO_2}/M_{TiO_2}) \quad (1)$$

where ρ and M are the density and molar mass of the corresponding material, respectively. All these samples were denoted as X %Ag−TiO_2, and X % is the atomic ratio of Ag in the composite, defined as $X\% = N_{Ag}/(N_{Ag} + N_{Ti})$, where N_{Ag} and N_{Ti} represent the number of Ag and Ti atoms in the composite. In this study, X % was designed to be 0, 5, 10, 15, and 20%, respectively. The corresponding deposition rates of Ag and TiO_2 are listed in Table 1. A total QCM thickness reading of 2 μm was reached at the end of each deposition, that is

$$d_{Ag}^{QCM} + d_{TiO_2}^{QCM} = 2\mu m \quad (2)$$

After the deposition, the nanorod samples were annealed in an argon atmosphere in a quartz tube furnace (Lindberg/Blue M Company) with an argon flow rate of 230 SCCM. During the annealing, the samples were heated to 400 and 500 °C, respectively, at a heating rate of 5 °C/min and subsequently annealed for 4 h. Then, the samples were cooled to room temperature in argon atmosphere. These processes could prevent the oxidation of Ag in the composite.

The morphologies and compositions of the nanorod arrays were characterized by a field-emission scanning electron microscope (SEM) equipped with an energy dispersive X-ray spectroscopy (EDX) (FEI Inspect F). Each sample was analyzed by X-ray diffraction (XRD) (PANanalytical X'Pert PRO) to confirm the crystal structures, using Cu Kα radiation with the X-ray incident angle of 0.5°. The optical properties were characterized by an UV−vis NIR double beam spectrophotometer (JASCO V-570) equipped with two rotatable Glan Thompson polarizers (Thorlabs, Inc.). The photocatalytic activities of both Ag NP embedded TiO_2 and pure TiO_2 nanorod arrays were evaluated by the photocatalytic degradation of a 10 ppm Methylene Blue (MB; $C_{16}H_{18}ClN_3S$, Alfa Aesar, CAS No. 122965-43-9) aqueous solution, under ultraviolet (UV; BLAK-RAY, Model B 100AP), visible (250 W quartz halogen lamp: UtiliTech), and UV plus visible light irradiation. Typically, the prepared MB aqueous solution had a pH value of 6.2 at room temperature. The samples on glass substrates (8 mm × 25.4 mm) were placed into a 10 mm × 10 mm × 45 mm clear methacrylate cuvette, filled with 4.0 mL of 10 ppm MB aqueous solution. Prior to the irradiation, each sample was kept in the dark for 30 min, to ensure equilibrium of the dye adsorption on the surface of the photocatalysts. Then, the samples were exposed to different illumination conditions for 4 h. The UV light at a wavelength of 365 nm had a power density about 10 mW/cm^2 at the position of the cuvette, as measured by a UV power meter (Fisher Scientific, UVA-365), and the visible light with wavelength range of 400 to 800 nm had a power density about 65 mW/cm^2 at the position of the cuvette, as measured by a thermal optical power meter (Thorlabs PM100D/

Table 1. Composition and Morphology Parameters for the As-Deposited Samples

samples	r_{Ag}(Å/s)	r_{TiO_2}(Å/s)	predicted X %	measured X' %	height h (μm)	tilting angle β (°)
TiO_2	0	3.5	0%		1.48 ± 0.05	55 ± 2
5% Ag–TiO_2	0.1	3.5	5%	9.4 ± 0.5%	1.21 ± 0.04	57 ± 2
10% Ag–TiO_2	0.2	3.3	10%	15 ± 2%	1.18 ± 0.02	58 ± 1
15% Ag–TiO_2	0.3	3.1	15%	22 ± 1%	1.10 ± 0.03	59 ± 1
20% Ag–TiO_2	0.4	2.9	20%	25.7 ± 0.6%	1.08 ± 0.03	59 ± 1

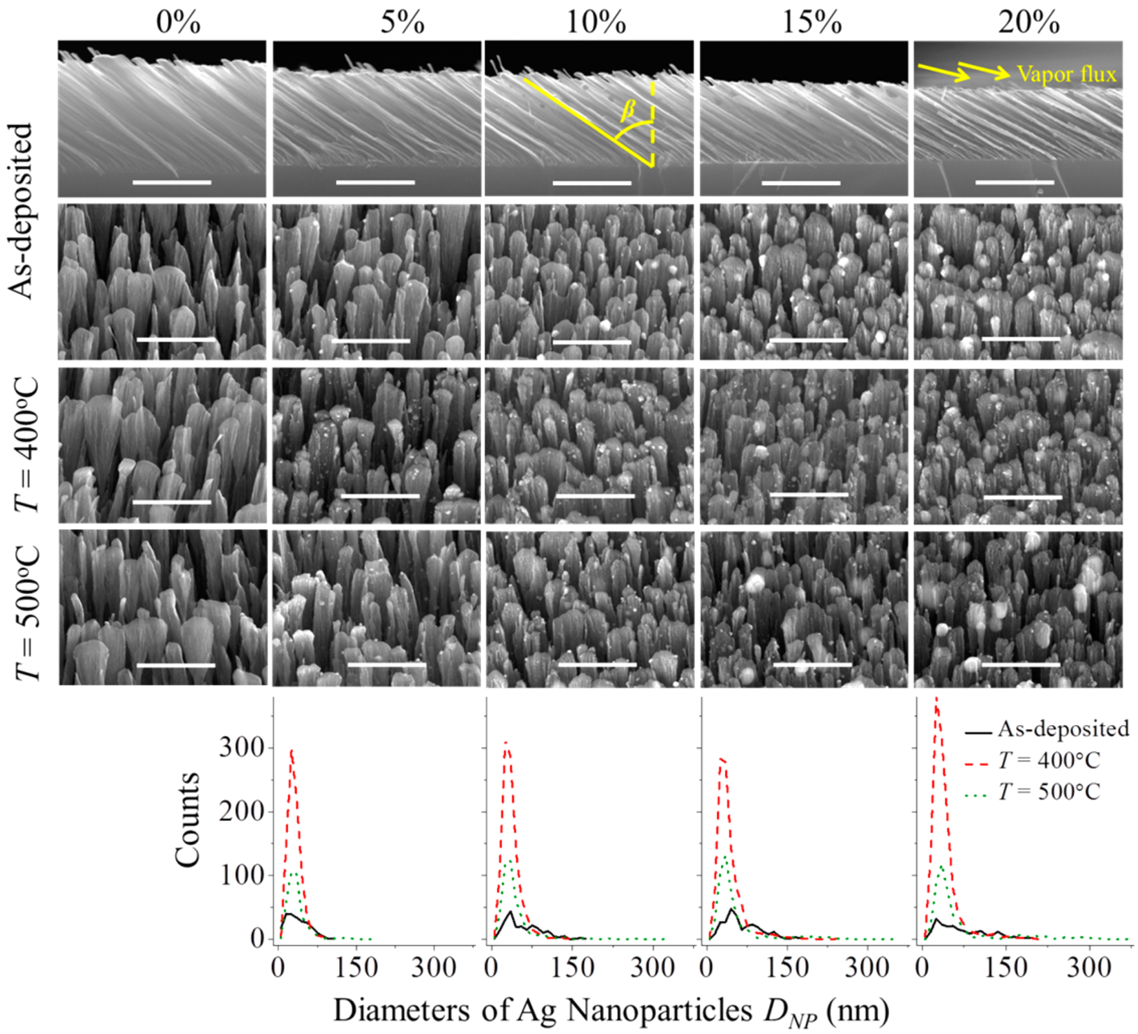

Figure 1. Representative SEM images of TiO_2 and Ag NP embedded TiO_2 composite nanorod arrays and the size distributions of Ag NPs. Scale bar in each SEM image represents 1 μm.

S310C). The position of the light sources was adjusted in such a way that the sample was facing toward the UV light and opposite to the visible light source. A water filter was placed near the cuvette on the visible light source side to absorb the IR radiation. Then, the degradation of MB aqueous solution was quantified by recording the optical absorption spectra of the remaining MB solution every 30 min in situ using a USB 2000 Ocean Optics spectrophotometer. The time evolution of absorbance peak at λ = 664 nm was used to evaluate the photodecay rate.

3. RESULTS

3.1. Composition of Ag–TiO_2 Nanocomposites. The qualitative composition of the Ag NP embedded TiO_2 samples were determined by EDX measurements. The EDX spectra of as-deposited samples are shown in Figure S1 in Supporting Information (Part I). The results along with the deposition conditions are summarized in Table 1. As shown in Table 1, the EDX measurements confirm that the measured Ag atomic ratio X' % have the same trend with the designed X %, but X' % is always larger than X %. In this paper, the designed Ag atomic ratio in the composite X % will be used throughout the context to refer to the nanorod samples.

3.2. Morphology of Ag–TiO_2 Composite Nanorod Arrays. The representative top view and cross-sectional view SEM images of as-deposited and annealed Ag–TiO_2 composite samples are shown in Figure 1. High-resolution top-view SEM images are presented in Supporting Information (Part II). For as-deposited films, as indicated by the SEM images (first two rows in Figure 1), tilted nanorod arrays are formed on the substrates with different doping concentrations of Ag. The nanorod density is estimated to be approximately 9 ± 1 rods/

μm^2 for each sample. The nanorods fan out along the direction perpendicular to the incident vapor flux due to the lack of shadowing effect in this direction.[34] The width at the top of nanorods along the fan-out direction is approximately 300 ± 100 nm, while the width perpendicular to the fan-out direction is approximately 50 ± 10 nm for all the as-deposited samples. From the cross-sectional view SEM images, the tilting angles β, defined as the angle of nanorod with respect to the surface normal of substrate and the vertical heights h of the as-deposited nanorods are measured and summarized in Table 1, and are plotted versus X' % in Figure 2. The tilting angle β is about 55° for the intrinsic TiO_2 nanorods and gradually increases with X' %, finally reaching 71° for pure Ag nanorods.[35] Based on a semiempirical statistic model that describes the tilting angle of composite nanorods,[36] by assuming that the effective radii of Ag atom and TiO_2 molecule are 145 and 200 pm, respectively, the β of the composite nanorods can be expressed as

$$\beta = 39.33(X'\%)^3 - 66.06(X'\%)^2 + 42.65X'\% + 54.96. \tag{3}$$

As shown in Figure 2, the fitting by the statistic model agrees well with the experimental data. The increase of Ag concentration in TiO_2 nanorods also leads to smaller vertical nanorod heights, as plotted in Figure 2. The heights of the nanorods h can be fitted by a model assuming that the contribution of each material is proportional to the QCM thickness d^{QCM}

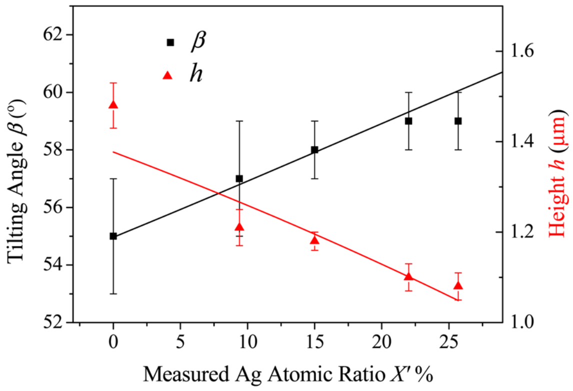

Figure 2. Nanorod tilting angle β and height h versus the measured Ag atomic ratio X' %.

$$h = h_{Ag} + h_{TiO_2} = A_{Ag}d_{Ag}^{QCM} + B_{TiO_2}d_{TiO_2}^{QCM} \tag{4}$$

where A_{Ag} and B_{TiO_2} are coefficients related to deposition conditions. Combined with eqs 1 and 2, the final expression for h in terms of X' % is

$$h = A_{Ag}\frac{1.08X'}{100 - 0.46X'} + B_{TiO_2}\left(2 - \frac{1.08X'}{100 - 0.46X'}\right) \tag{5}$$

However, the best fitting gives $A_{Ag} = -0.4 \pm 0.2$ and $B_{TiO_2} = 0.68 \pm 0.03$. An explanation for the negative A_{Ag} value is that Ag atoms are incorporated into TiO_2 voids and reduce the porosity of the composite nanorods, as we can see in later discussion for TEM results. After the composite nanorods annealed in argon, there is no distinct change in β and h.

From these SEM images, Ag NPs are observable on the surface of the nanorods. The average sizes or diameters, D_{NP}, and densities, n_{NP}, defined as the particle numbers per unit surface area of nanorods of these nanoparticles under different thermal treatments are summarized in Table 2, and the particle size distributions are plotted in the bottom row of Figure 1. In the as-deposited samples, only a few nanoparticles can be observed. After annealing in argon at T = 400 °C, the nanoparticle densities increase dramatically, especially in the small size range (<70 nm) and decrease significantly after annealing at T = 500 °C. In addition, larger Ag NPs can be observed after annealing at T = 500 °C. From the statistics on Ag NPs, we find the following general trend: for the samples under the same thermal treatment condition, the average particle size increases with X %; in the meantime, the variation of particle size becomes larger. These Ag NPs are formed through the diffusion and the coalescence of silver atoms or clusters. The diffusion and coalescence of metal nanoparticles has already been studied,[37] which indicates that the high surface energy of small metal particles leads to the coalescence of particles in order to minimize the total surface energy. The energy for the diffusion and coalescence of metal particles mainly comes from the substrate temperature. During the deposition, the substrate temperature was increased to less than

Table 2. Sizes and Densities of Ag Nanoparticles on Surfaces of Nanorods, Average Grain Sizes for TiO_2 Anatase Phase for the Annealed Samples and the Specific Photodegradation Rates, the Temperature Increase on the Surface of Nanorods Calculated by Eq S14, and the Photocatalytic Reaction Enhancement Factors for the Samples Annealed at T = 500°C

samples		TiO_2	5% Ag –TiO_2	10% Ag–TiO_2	15% Ag–TiO_2	20% Ag–TiO_2
as-deposited	D_{NP} (nm)		40 ± 20	60 ± 30	70 ± 30	70 ± 50
	n_{NP} (μm^{-2})		5.3	5.4	6.6	5.3
T = 400°C	D_{NP} (nm)		30 ± 10	50 ± 20	50 ± 20	50 ± 30
	n_{NP} (μm^{-2})		19.8	23.9	24.5	30.0
	TiO_2 grain size (nm)	28.8 ± 0.9	30 ± 1	23.7 ± 0.6	24.2 ± 0.9	24.5 ± 0.9
	k'_{UV-vis} (h^{-1} μm^{-1})	0.124	0.141	0.088	0.063	0.059
T = 500°C	D_{NP} (nm)		40 ± 20	40 ± 30	50 ± 50	70 ± 70
	n_{NP} (μm^{-2})		8.5	10.6	11.6	11.4
	TiO_2 grain size (nm)	29.0 ± 0.8	32.2 ± 0.8	24.6 ± 0.5	26.8 ± 0.7	24.4 ± 0.6
	k'_{Vis} (h^{-1} μm^{-1})	0.013	0.023	0.028	0.020	0.018
	k'_{UV} (h^{-1} μm^{-1})	0.083	0.088	0.1006	0.114	0.086
	k'_{UV-vis} (h^{-1} μm^{-1})	0.150	0.157	0.170	0.179	0.154
	local temperature increase ΔT_{tot} (K)		0.45	0.57	1.2	3.2
	$EF = k'_{UV-vis}/k'_{UV}$	1.81	1.79	1.69	1.57	1.78

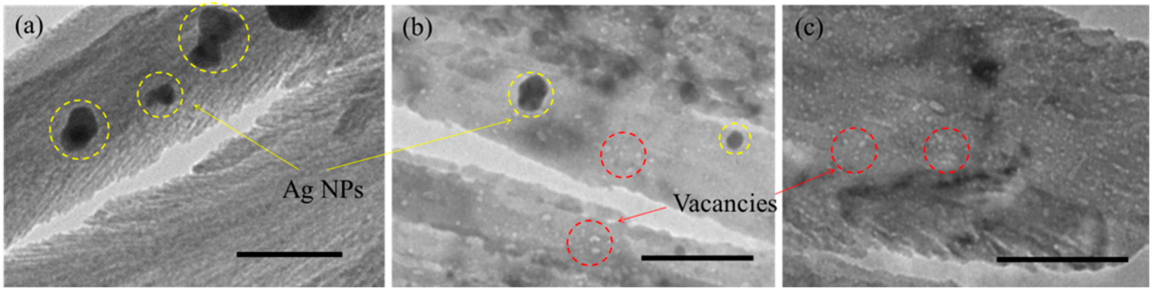

Figure 3. Representative TEM images of 20% Ag–TiO_2 nanorods (a) as-deposited and (b) annealed at T = 500 °C and (c) TiO_2 nanorods annealed at T = 500 °C. Ag NPs and vacancies are labeled by yellow and red circles, respectively. Each scale bar represents 100 nm.

100 °C. Moreover, the silver can be easily oxidized during the co-deposition where oxygen species are present. It is known that oxidation occurs on the surface of Ag NPs even at room temperature when exposed to oxygen.[38] Therefore, during the deposition, the diffusion and coalescence of Ag clusters or nanoparticles may be limited by both the low substrate temperature and potentially the formation of silver oxide film on Ag NPs or clusters. As a result, most of the Ag atoms or clusters are hidden within the TiO_2 matrix and cannot diffuse out to the surface to form large nanoparticles in as-deposited samples, and they could be too small to be seen in SEM. This may explain why only a few nanoparticles can be observed on the as-deposited samples.

The annealed nanorods have more and larger nanoparticles than as-deposited nanorods because the high temperature during the annealing process provides sufficient energy for the diffusion and coalescence of Ag NPs. High temperature also enables the thermal decomposition of silver oxide into metallic silver and oxygen,[39] which is in favor of diffusion and coalescence. We propose that the annealing process segregates the Ag atoms from TiO_2 matrix, allows the migration to the surface of TiO_2 nanorods, and results in aggregation into larger clusters or particles by coalescence, forming new nanoparticles on the surface. The Ag NPs on the surface can also grow up through Ostwald ripening or coalescence. During the annealing process at T = 400 °C, the prevailing process is the migration of Ag to the surface and the formation of new particles through coalescence. This results in a significant increase of the particle density. The annealing temperature 400 °C may limit further coalescence, leading to a narrow size distribution between 20 and 70 nm. The annealing at a higher temperature T = 500 °C provides more thermal energy, thus enabling further diffusion of Ag atoms and coalescence of Ag NPs. The coalescence and Ostwald ripening of Ag NPs on the surface is the prevailing process and results in larger Ag NPs (>150 nm) and smaller Ag NP densities on the surface.

The particle distribution of Ag–TiO_2 composite is also confirmed by TEM measurement. The representative TEM images of as-deposited and annealed 20% Ag–TiO_2 (500 °C) and annealed TiO_2 (500 °C) samples are shown in Figure 3. The Ag NPs can be clearly observed from the TEM images, as labeled by the yellow circles. Before annealing, each nanorod backbone exhibits fibrous structures, which have been observed in previous study.[40] But after annealing at 500 °C in argon, fibrous structures are hardly observable. Instead, many vacancies appear on the intrinsic TiO_2 nanorods, as labeled by the red circles in Figure 3b,c. We believe that vacancies already exist in the as-deposited fibrous TiO_2 nanorods and become large through diffusion and coalescence during the crystallization of TiO_2.

3.3. XRD Characterization. The XRD spectra of both pure TiO_2 and Ag NP embedded TiO_2 nanorods were taken to confirm the crystal structures of the composites, as shown in Figure 4. For the as-deposited samples, Figure 4a shows no diffraction peaks associated with crystalline TiO_2, demonstrating that TiO_2 in both the as-deposited intrinsic and composite samples are amorphous. There are very weak diffraction peaks associated with Ag observed at 2θ = 38.1°, 44.3°, 64.5°, and

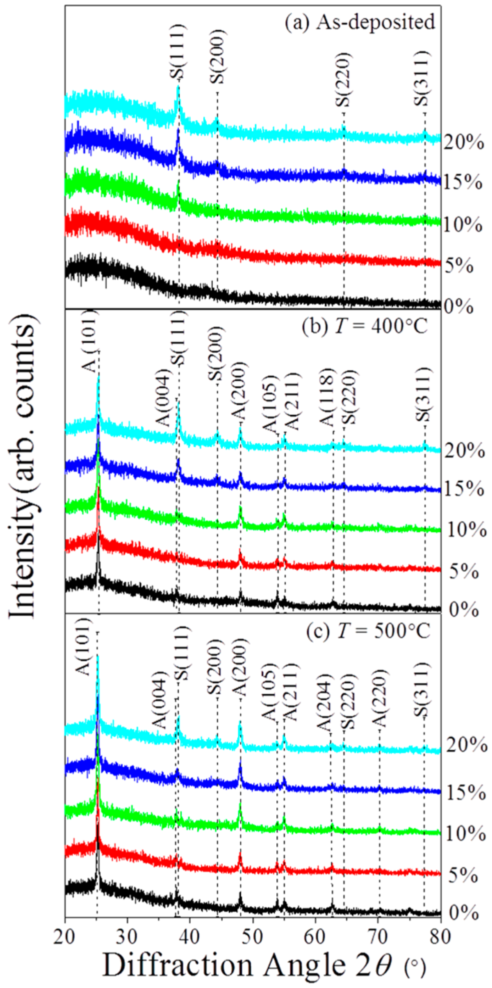

Figure 4. XRD spectra of TiO_2 and Ag NP embedded TiO_2 composite nanorod arrays: (a) as-deposited, (b) annealed at T = 400 °C, and (c) annealed at T = 500 °C. The symbol "A" and "S" represent the XRD peaks of anatase TiO_2 and crystalline Ag, respectively.

77.4° in Ag NP embedded TiO_2 samples, corresponding respectively to the (111), (200), (220), and (311) crystal planes of Ag. The peaks become more intense as X % increases. No diffraction peaks of silver oxide are observed, indicating either that there is a very small amount of silver oxide in as-deposited samples, which is beyond the detection limit of the instrument, or the silver oxides are in amorphous state.

After annealing at 400 and 500 °C in argon, the diffraction peaks corresponding to TiO_2 anatase phase are observed at 2θ = 25.3°, 37.8°, 48.1°, 53.9°, 55.1°, 62.7°, 68.8°, 70.2°, and 77.4°, corresponding respectively to the (101), (004), (200), (105), (211), (204), (116), (220), and (215) crystal planes of TiO_2 anatase phase, as shown in Figure 4b,c. The diffraction peak positions of Ag almost remain the same, while the diffraction intensities become more significant demonstrating more Ag are forming crystal clusters compared to as-deposited samples. This observation is consistent with SEM and TEM observations and indicates that part of Ag and TiO_2 are incorporated in amorphous state, while part of the Ag aggregates into small crystals for the as-deposited samples.

By applying Scherrer's formula, the average grain sizes of TiO_2 were estimated using the strongest peaks (101) for anatase and are summarized in Table 2. Higher annealing temperature leads to larger grain sizes, except for the 20% Ag–TiO_2 samples. It has been widely accepted that the presence of silver in the TiO_2 matrix has an inhibition effect on the growth of anatase phase.[41−43] However, in our case, only high Ag concentration (10, 15, 20%) leads to a smaller anatase grain size than pure TiO_2. It is surprising to observe that 5% Ag–TiO_2 has a larger grain size than pure TiO_2. The reason for the increase of the anatase grain size at low Ag concentration is unknown.

3.4. Optical Properties.

The optical properties of TiO_2 and Ag–TiO_2 nanorod arrays were characterized by UV–vis spectroscopy. Figure 5 shows the extinction spectra, extracted from transmission spectra of both intrinsic TiO_2 and Ag–TiO_2 nanorod films with unpolarized incident light. For all the as-deposited or annealed samples, strong extinction in UV region is primarily attributed to the absorption of TiO_2. Moreover, Ag loading and annealing conditions also affect the extinction spectra.

For all the as-deposited composite samples, no distinct feature of LSPR of Ag NPs is observed possibly due to low density of Ag NPs. The extinction in the visible region increases with increasing Ag concentration, though the film thickness decreases monotonically. It keeps almost the same trend in the UV region except for the 10% Ag–TiO_2 sample. This increase of extinction over the broad spectrum is mainly attributed to the absorption and scattering of Ag atoms and nanoparticles in as-deposited films.

After the samples are annealed in argon, the extinction spectra of TiO_2, 5%, and 10% Ag–TiO_2 composite samples almost overlap with each other in the visible region. However, a very broad extinction peak is observed in the wavelength range of 500–700 nm in the spectra of 15% and 20% Ag–TiO_2 samples due to LSPR of metallic Ag NPs. The position of the LSPR peak of Ag NPs is determined by both their size and the refractive index of the host matrix. A broad LSPR peak results from a wide distribution of Ag nanoparticle sizes. In addition, the samples annealed at 400 °C have a more intense extinction peak around 600 nm than those annealed at 500 °C. This is mainly due to the fact that the density of Ag NPs annealed at 400 °C is much higher than that annealed at 500 °C, as shown in Figure 1.

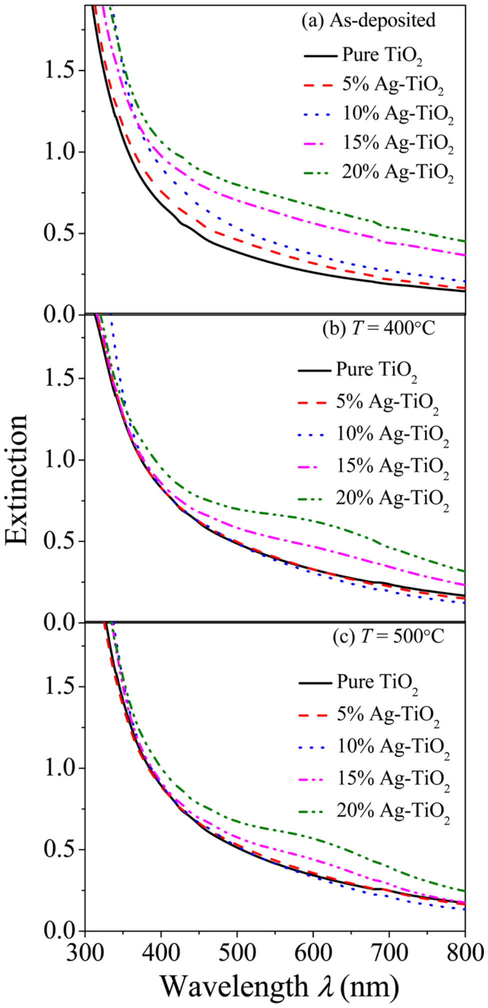

Figure 5. Unpolarized optical extinction spectra of both TiO_2 and Ag–TiO_2 nanorod arrays: (a) as-deposited, (b) annealed at T = 400 °C, and (c) annealed at T = 500 °C.

The optical properties of TiO_2 and Ag–TiO_2 nanorod films can be estimated using an effective medium theory (EMT).[44] The EMT of oblique columnar structures has already been well-developed.[45,46] Maxwell–Garnett (MG) approximation is first used to estimate the effective refractive index of the bulk TiO_2 with the Ag NP composite, and then a Bruggeman (Br) approximation is applied to estimate the effective refractive index of the Ag–TiO_2 nanorod arrays (i.e., the void Ag–TiO_2 composite structures. The nanorods can be treated as prolate spheroids. The detailed calculations are presented in the Supporting Information (Part III), and the calculated absorption spectra are plotted in Figure 6. As demonstrated by the calculations, a distinct absorption peak centered at about 550 nm appears in the spectra of all Ag–TiO_2 composite nanorod films, and it becomes more intense as the concentration of silver increases. This is consistent qualitatively with the experimental data. It should be noted that this EMT calculation only considers the porosity and composition of the materials and uses the bulk optical constants of both Ag and TiO_2. However, Ag NPs' optical constants depend on the NP sizes.[47,48] Since the LSPR wavelength red shifts with the NP size and the Ag NP size distribution are very broad, as shown in

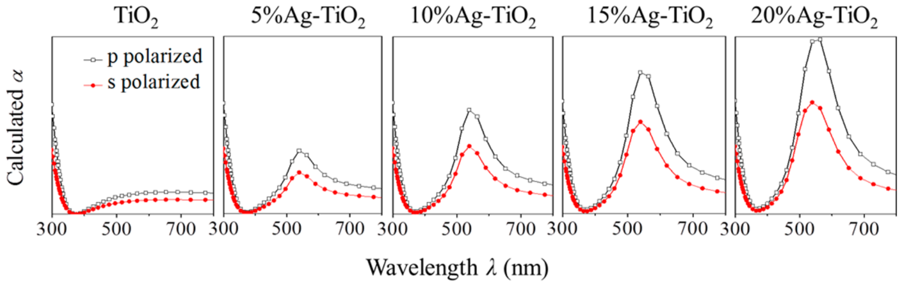

Figure 6. Absorption coefficient predicted by EMT.

Figure 1, one shall not expect sharp LSPR peaks in the absorption spectra, rather broad peaks, or even no peaks. Therefore, the EMT calculation results cannot accurately match the experimental results, as shown in Figure 5. However, we believe that the calculated spectra should give some qualitative information or trend on how the optical properties change with Ag composition, regardless of the LSPR peaks. Indeed, although the calculated spectral shapes are very different from the experimental spectra, the predicted trend is similar.

3.5. Photocatalytic Activity. In order to study the effect of Ag loading in TiO$_2$ on the photocatalytic activities, MB photodegradation experiments were performed under UV, visible, and UV−visible illuminations. The absorption spectra of MB solution were monitored over 4 h, and the change in the intensity of the MB absorption peak at $\lambda = 664$ nm is used to determine the decay rates by fitting the data to a pseudo-first-order decay equation

$$\ln\frac{\alpha(0)}{\alpha(t)} = kt \tag{6}$$

where $\alpha(0)$ and $\alpha(t)$ are the absorbance of MB at time $t = 0$ and t, and k is the decay rate. Figure 7 shows the plots of $\ln[\alpha(0)/\alpha(t)]$ versus t for different X %Ag−TiO$_2$ composite nanorods annealed at 500 °C, and the solid lines are the fitting results under visible illumination. As described above, the increase in X % results in less TiO$_2$, shorter nanorods, and less surface area. In order to remove the effect of the surface area and only account for the effect of the Ag loading, the specific decay rate k', which is the decay rates k normalized by the average lengths of nanorods, is obtained. Here, we assume that the decay rates are linearly proportional to the average nanorod length l,[49] which can be obtained by $l = h/\cos\beta$. The obtained specific decay rates are summarized in Table 2. Both the TiO$_2$ and Ag−TiO$_2$ samples annealed at 400 °C exhibit lower photocatalytic activity than those annealed at 500 °C under UV−vis illumination. Therefore, in this work, we will focus on how to improve the photocatalytic activity of samples annealed at 500 °C. The specific decay rates of the samples annealed at 500 °C are shown in Figure 8. It is clear that $k'_{\text{UV−vis}} > k'_{\text{UV}} + k'_{\text{Vis}}$ for all the Ag−TiO$_2$ samples. Under the same illumination, with increasing X %, the specific decay rate k' increases, reaches the maximum, and then decreases. k' reaches the maximum at X % = 15% under UV and UV−vis illuminations and at X % = 10% under visible illumination.

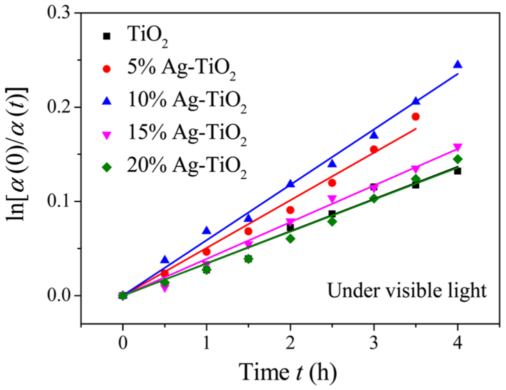

Figure 7. Photocatalytic MB degradation kinetics under visible light illumination for the samples annealed at T = 500 °C.

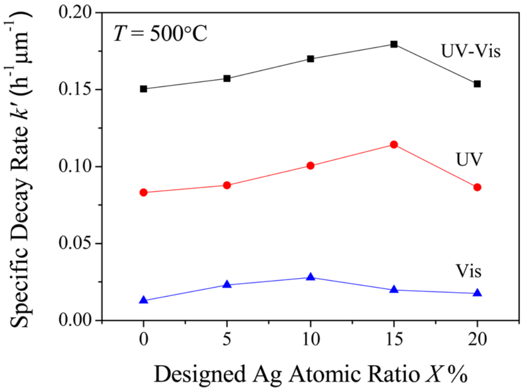

Figure 8. Specific photodegradation rate k' of the samples annealed at T = 500 °C under different illumination versus the designed Ag atomic ratio X %.

Under visible illumination, though TiO$_2$ cannot be activated due to its large band gap, the decay rate is not zero and is mainly due to the self-photosensitization of MB.[50] The MB molecules can be activated by visible light. Then the excited electrons may be subsequently transferred into the conduction band of TiO$_2$ and react with the preadsorbed oxygen on the surface of TiO$_2$, producing oxidizing species which may participate in the reaction of MB photodegradation.[51] Compared to the pure TiO$_2$, the Ag−TiO$_2$ samples exhibit better photocatalytic performance under visible illumination. There are three possible mechanisms for such an observation. First, Ag NPs can absorb visible light due to LSPR and then inject the excited electrons into the conduction band of TiO$_2$ as illustrated in Figure 9a. When the concentration of Ag is low, the increase of Ag loading results in larger interface area between TiO$_2$ and Ag, which facilitates the electron transfer and enhances the photocatalytic activity. However, as more Ag is loaded on TiO$_2$, less TiO$_2$ is exposed to MB molecules, which results in less electrons transferred from MB to TiO$_2$ and thus reduces the photocatalytic activity.

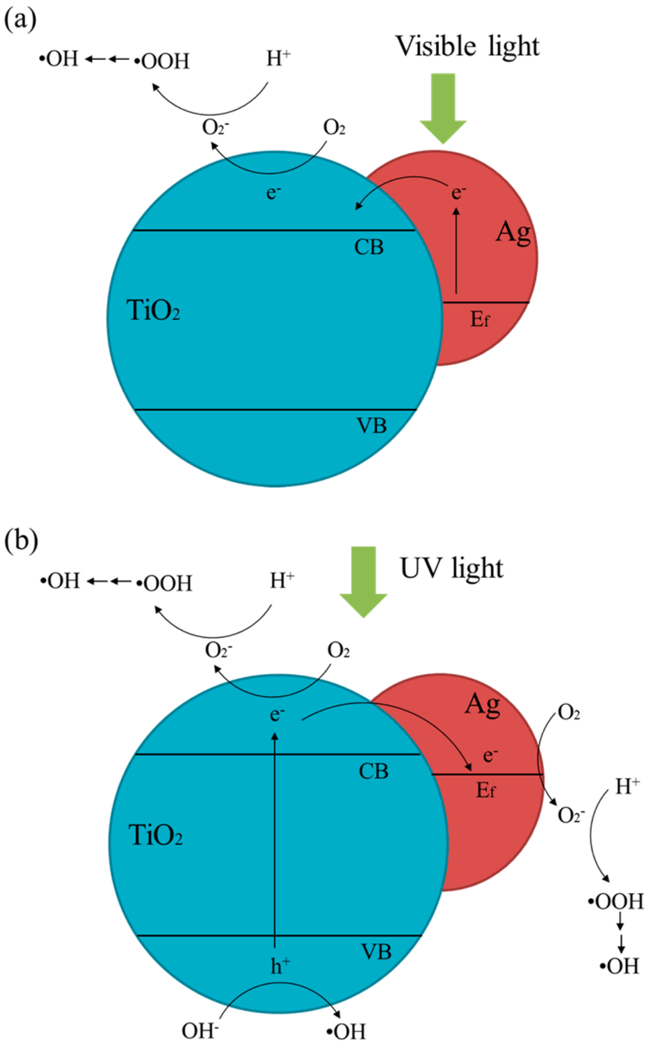

Figure 9. Schematics of photocatalytic mechanism: (a) under visible light and (b) under UV light. Here, the band bending caused by Schottky junction at the Ag−TiO_2 interface is not illustrated.

Another possible mechanism is that the energy is transferred from photoexcited Ag NPs to TiO_2 in a radiative way through the interaction of TiO_2 with localized enhanced electric field, resulting in an increase of the electron−hole pair density.[19] However, if the energy of LSPR is lower than the band gap of TiO_2, no significant enhancement in photocatalytic activity can be observed.[52] As shown in the extinction spectra, the LSPR wavelength of Ag NPs is located between 500 and 700 nm, which is insufficient to activate TiO_2. Therefore, this radiative energy transfer may not lead to the enhanced photocatalytic activity.

Finally, Ag NPs can generate heat under optical illumination due to nonradiative decay of surface plasmons into phonon modes. The localized heating and the temperature increase may contribute to the enhanced photocatalytic activity. The temperature increase ΔT_{tot} due to plasmon resonance can be estimated by a theory developed by Govorov et al. and is summarized in Table 2.[53] The calculation details can be found in Supporting Information (Part IV). With Ag concentration, ΔT_{tot} increases and reaches 3.2 K for 20% Ag−TiO_2. If the localized heating is the dominant mechanism in the photodegradation of MB, 20% Ag−TiO_2 should have the highest decay rate, which does not occur in our experiment. So we assume that the localized heating by Ag NPs is negligible and does not contribute significantly to the enhanced photocatalytic activity.

Upon UV illumination, TiO_2 is activated and generates electron−hole pairs. When Ag is loaded in TiO_2 matrix, the electrons in the conduction band of TiO_2 may be trapped by Ag NPs,[54] which is energetically favorable and suppresses the electron−hole recombination, as illustrated in Figure 9b. In addition, the accumulation of the trapped electrons in Ag NPs shifts the Fermi level more negative and makes Ag more reductive. The photogenerated electrons in TiO_2 and the trapped electrons in Ag react with the preadsorbed oxygen. The holes in the valence band of TiO_2 react with H_2O or OH^-. Both reactions finally generate hydroxyl radicals, as illustrated in Figure 9b,[51] which then degrade MB. Compared to the degradation under visible illumination in which electrons from MB and Ag play an important role, the degradation of MB under UV illumination is much faster because the TiO_2 matrix can generate more electron−hole pairs, and both electrons and holes contribute to the degradation. More Ag loaded in TiO_2 increases the interface area and results in better charge separation and thus better photocatalytic activity. The highest photocatalytic activity was observed with 15% Ag−TiO_2 under UV illumination. However, a higher concentration of Ag leads to decreased photocatalytic activity. As shown in the SEM images, 20% Ag−TiO_2 has more large Ag NPs than 15% Ag−TiO_2, limiting the exposure area of TiO_2 to UV illumination and MB molecules. Moreover, as more photogenerated electrons are accumulated in Ag, the probability of holes captured by these negatively charged nanoparticles increases significantly and decreases the efficiency of electron−hole separation, subsequently reducing the photocatalytic activity.

Under UV−visible illumination, faster degradation occurs for each sample compared with that under UV light. The visible light can excite both MB molecules and Ag NPs, resulting in self-photosensitization and hot electrons transferred to conduction band of TiO_2, respectively. In order to see the effect of the addition of visible light, the enhancement factor EF, defined as $EF = k'_{UV-vis} / k'_{UV}$ is calculated for each sample and presented in Table 2. The EF is inversely related to the specific decay rate under visible illumination, which means a better photocatalytic performance under visible illumination will lead to a smaller enhancement under UV−visible illumination. For the intrinsic TiO_2 sample, the maximum enhancement is achieved and is only due to the self-sensitization of MB. For the Ag−TiO_2 composite samples, the electron transfer has a different direction under UV or visible illumination. When Ag−TiO_2 composite samples are under the illumination of both UV and visible light, the photogenerated electrons in the conduction band of TiO_2 can be trapped at Ag NPs and thus improve the lifetime of the holes in the valence band of TiO_2. In the meantime, Ag can also be excited by visible light and transfer electrons back to TiO_2, which prevents the charge separation in TiO_2 and leads to a negative impact on the photocatalytic activity.

4. CONCLUSION

Ag−TiO_2 composite nanorod arrays with different Ag concentrations have been fabricated by oblique angle co-deposition. TiO_2 is amorphous in the as-deposited samples and changes into anatase after annealing. As indicated by SEM and TEM images, Ag NPs are formed on and inside the TiO_2 matrix. By varying the concentration of Ag and the annealing condition, the size and the density of Ag NPs on the surface of TiO_2 can be tuned and, subsequently, also their optical properties. The addition of Ag in TiO_2 results in enhanced photocatalytic activity compared to pure TiO_2. Ag NPs play different roles in enhancing photocatalytic activity under different light sources. Under visible illumination, the Ag NPs are excited due to LSPR, and the electron transfer from Ag to TiO_2 is the primary contribution to the enhancement in photocatalytic activity. Under UV illumination, TiO_2 is activated and electron−hole pairs are generated, and Ag NPs work as electron traps, facilitating the charge separation and thus enhancing the photocatalytic activity. However, extra Ag loading beyond the optimal concentration leads to reduced photocatalytic activity mainly due to limited TiO_2 surface area exposed to dye molecules and the increased possibility of capture of holes by Ag NPs. Since the electron transfers are in the opposite direction under UV and visible illumination, the direct contact of Ag with TiO_2 may not result in a great enhancement in the photocatalytic performance. In order to improve the photocatalytic activity under UV−vis illumination, indirect contact of TiO_2 with Ag may be necessary to get rid of the back transfer of electrons to Ag.

■ ASSOCIATED CONTENT

Ⓢ Supporting Information

EDX spectra of Ag−TiO_2 composite nanorod arrays, high-resolution top-view SEM images of Ag−TiO_2 nanorod arrays, estimation of optical properties of Ag−TiO_2 nanorod arrays by effective medium theory, and estimation of the temperature increase of Ag NPs on TiO_2 nanorod under visible light. This material is available free of charge via the Internet at http://pubs.acs.org.

■ AUTHOR INFORMATION

Corresponding Author

*E-mail: yizhuohe@physast.uga.edu. Tel.: (706) 542-6230. Fax: (706) 542-2492.

Notes

The authors declare no competing financial interest.

■ ACKNOWLEDGMENTS

We gratefully acknowledge the support from Savannah River National Laboratory LDRD-DOE program and partial support from the National Science Foundation (Grant No. ECCS-1029609).

■ REFERENCES

(1) Fujishima, A.; Honda, K. *Nature* **1972**, *238*, 37−38.

(2) Szymanski, P.; El-Sayed, M. A. *Theor. Chem. Acc.* **2012**, *131*, 1202.

(3) Ni, M.; Leung, M. K. H.; Leung, D. Y. C.; Sumathy, K. *Renewable Sustainable Energy Rev.* **2007**, *11*, 401−425.

(4) Inoue, T.; Fujishima, A.; Konishi, S.; Honda, K. *Nature* **1979**, *277*, 637−638.

(5) Indrakanti, V. P.; Kubicki, J. D.; Schobert, H. H. *Energy Environ. Sci.* **2009**, *2*, 745.

(6) Koci, K.; Obalova, L.; Lacny, Z. *Chem. Pap.* **2008**, *62*, 1−9.

(7) Roy, S. C.; Varghese, O. K.; Paulose, M.; Grimes, C. A. *ACS Nano* **2010**, *4*, 1259−1278.

(8) Sato, S. *Chem. Phys. Lett.* **1986**, *123*, 126−128.

(9) Sato, S.; Nakamura, R.; Abe, S. *Appl. Catal., A* **2005**, *284*, 131−137.

(10) Borgarello, E.; Kiwi, J.; Gratzel, M.; Pelizzetti, E.; Visca, M. *J. Am. Chem. Soc.* **1982**, *104*, 2996−3002.

(11) Klosek, S.; Raftery, D. *J. Phys. Chem. B* **2001**, *105*, 2815−2819.

(12) Behar, D.; Rabani, J. *J. Phys. Chem. B* **2006**, *110*, 8750−8755.

(13) Oregan, B.; Gratzel, M. *Nature* **1991**, *353*, 737−740.

(14) Marci, G.; Augugliaro, V.; Lopez-Munoz, M. J.; Martin, C.; Palmisano, L.; Rives, V.; Schiavello, M.; Tilley, R. J. D.; Venezia, A. M. *J. Phys. Chem. B* **2001**, *105*, 1026−1032.

(15) Yamakata, A.; Ishibashi, T.; Onishi, H. *J. Phys. Chem. B* **2002**, *106*, 9122−9125.

(16) Zhang, L. W.; Mohamed, H. H.; Dillert, R.; Bahnemann, D. *J. Photochem. Photobiol., C* **2012**, *13*, 263−276.

(17) Henderson, M. A. *Surf. Sci. Rep.* **2011**, *66*, 185−297.

(18) Tian, Y.; Tatsuma, T. *J. Am. Chem. Soc.* **2005**, *127*, 7632−7637.

(19) Awazu, K.; Fujimaki, M.; Rockstuhl, C.; Tominaga, J.; Murakami, H.; Ohki, Y.; Yoshida, N.; Watanabe, T. *J. Am. Chem. Soc.* **2008**, *130*, 1676−1680.

(20) Chen, X.; Zheng, Z. F.; Ke, X. B.; Jaatinen, E.; Xie, T. F.; Wang, D. J.; Guo, C.; Zhao, J. C.; Zhu, H. Y. *Green Chem.* **2010**, *12*, 414−419.

(21) Armelao, L.; Barreca, D.; Bottaro, G.; Gasparotto, A.; Maccato, C.; Tondello, E.; Lebedev, O. I.; Turner, S.; Van Tendeloo, G.; Sada, C.; Stangar, U. L. *ChemPhysChem* **2009**, *10*, 3249−3259.

(22) Gong, D.; Ho, W. C. J.; Tang, Y.; Tay, Q.; Lai, Y.; Highfield, J. G.; Chen, Z. *J. Solid State Chem.* **2012**, *189*, 117−122.

(23) Smith, W.; Mao, S.; Lu, G. H.; Catlett, A.; Chen, J. H.; Zhao, Y. P. *Chem. Phys. Lett.* **2010**, *485*, 171−175.

(24) Kedziora, A.; Strek, W.; Kepinski, L.; Bugla-Ploskonska, G.; Doroszkiewicz, W. *J. Sol−Gel Sci. Technol.* **2012**, *62*, 79−86.

(25) Lee, M. S.; Hong, S.-S.; Mohseni, M. *J. Mol. Catal. A: Chem.* **2005**, *242*, 135−140.

(26) He, Y. P.; Zhao, Y. P.; Wu, J. S. *Appl. Phys. Lett.* **2008**, *92*, 063107.

(27) He, Y. P.; Zhang, Z. Y.; Hoffmann, C.; Zhao, Y. P. *Adv. Funct. Mater.* **2008**, *18*, 1676−1684.

(28) Larsen, G. K.; Fitzmorris, R.; Zhang, J. Z.; Zhao, Y. P. *J. Phys. Chem. C* **2011**, *115*, 16892−16903.

(29) Larsen, G. K.; Fitzmorris, B. C.; Longo, C.; Zhang, J. Z.; Zhao, Y. P. *J. Mater. Chem.* **2012**, *22*, 14205−14218.

(30) He, Y. P.; Brown, C.; He, Y. Z.; Fan, J. G.; Lundgren, C. A.; Zhao, Y. P. *Chem. Commun.* **2012**, *48*, 7741−7743.

(31) He, Y. P.; Brown, C.; Lundgren, C. A.; Zhao, Y. P. *Nanotechnology* **2012**, *23*, 365703.

(32) He, Y.; Fan, J. G.; Zhao, Y. P. *Cryst. Growth Des.* **2010**, *10*, 4954−4958.

(33) He, Y. P.; Zhao, Y. P. *Nanoscale* **2011**, *3*, 2361−2375.

(34) van Popta, A. C.; Cheng, J.; Sit, J. C.; Brett, M. J. *J. Appl. Phys.* **2007**, *102*, 013517.

(35) Driskell, J. D.; Shanmukh, S.; Liu, Y.; Chaney, S. B.; Tang, X. J.; Zhao, Y. P.; Dluhy, R. A. *J. Phys. Chem. C* **2008**, *112*, 895−901.

(36) Zhao, Y.; He, Y.; Brown, C. *Appl. Phys. Lett.* **2012**, *100*, 033106.

(37) Jose-Yacaman, M.; Gutierrez-Wing, C.; Miki, M.; Yang, D. Q.; Piyakis, K. N.; Sacher, E. *J. Phys. Chem. B* **2005**, *109*, 9703−9711.

(38) Cai, W.; Zhong, H.; Zhang, L. *J. Appl. Phys.* **1998**, *83*, 1705.

(39) Garner, W. E.; Reeves, L. W. *Trans. Faraday Soc.* **1954**, *50*, 254−260.

(40) He, Y. P.; Zhang, Z. Y.; Zhao, Y. P. J. *J. Vac. Sci. Technol., B: Microelectron. Nanometer Struct.–Process., Meas., Phenom.* **2008**, *26*, 1350.

(41) Chao, H. E.; Yun, Y. U.; Xingfang, H. U.; Larbot, A. *J. Eur. Ceram. Soc.* **2003**, *23*, 1457−1464.

(42) Li, X.; Wang, L.; Lu, X. *J. Hazard. Mater.* **2010**, *177*, 639−647.

(43) Park, J.-Y.; Hwang, K.-J.; Lee, J.-W.; Lee, I.-H. *J. Mater. Sci.* **2011**, *46*, 7240−7246.

(44) Choy, T. *Effective Medium Theory: Principles and Applications*; Oxford University Press: New York, 1999.

(45) Smith, G. B. *Opt. Commun.* **1989**, *71*, 279−284.

(46) Smith, G. B. *Appl. Opt.* **1990**, *29*, 3685.

(47) Doremus, R. H. *J. Chem. Phys.* **1965**, *42*, 414−417.

(48) Haynes, C. L.; Van Duyne, R. P. *J. Phys. Chem. B* **2001**, *105*, 5599−5611.

(49) Smith, W.; Ingram, W.; Zhao, Y. *Chem. Phys. Lett.* **2009**, *479*, 270−273.

(50) Chatterjee, D.; Dasgupta, S.; Rao, N. N. *Sol. Energy Mater. Sol. Cells* **2006**, *90*, 1013−1020.

(51) Wu, T. X.; Liu, G. M.; Zhao, J. C.; Hidaka, H.; Serpone, N. *J. Phys. Chem. B* **1998**, *102*, 5845−5851.

(52) Ingram, D. B.; Linic, S. *J. Am. Chem. Soc.* **2011**, *133*, 5202−5205.

(53) Govorov, A. O.; Zhang, W.; Skeini, T.; Richardson, H.; Lee, J.; Kotov, N. A. *Nanoscale Res. Lett.* **2006**, *1*, 84−90.

(54) Takai, A.; Kamat, P. V. *ACS Nano* **2011**, *5*, 7369−7376.